Geophys. J. Int. (2008) **173,** 753–765 doi: 10.1111/j.1365-246X.2008.03760.x

Geomagnetic dependence of ionospheric disturbances induced by tsunamigenic internal gravity waves

Giovanni Occhipinti,[1,2,3] E. Alam Kherani[1] and Philippe Lognonné[1]

[1] *Institut de Physique du Globe de Paris, UMR7154, France. E-mail: ninto@ipgp.jussieu.fr*
[2] *Office National d'Etudes et de Recherches Aérospatiales, France*
[3] *NASA-Jet Propulsion Laboratory, USA*

Accepted 2008 February 12. Received 2007 December 23; in original form 2007 August 23

SUMMARY

A series of ionospheric anomalies following the Sumatra tsunami has been recently reported in the literature. These anomalies show the signature in the ionosphere of tsunami-generated internal gravity waves (IGW) propagating in the neutral atmosphere over the ocean. All these anomalies, observed in the total electron content (TEC) measured by GPS or altimeters, show geographical heterogeneity in the perturbed TEC amplitude and suggest a dependence on geomagnetic latitude. This latitudinal dependence has been taken into account in the previous 3-D modelling used for the interpretation of the TEC Topex and Jason data. Here we present an accurate description of the ocean–atmosphere–ionosphere coupling method, and focus on the properties of the propagation of tsunamigenic IGW in the neutral atmosphere and their interaction with the ionospheric plasma. The analytical dependence on the geomagnetic field in the neutral–plasma coupling discussed in detail and quantitative modelling is used to describe the propagation of a simple tsunami wave at the global scale. What emphasize the role of geomagnetic field within the neutral–plasma coupling at the equatorial and mid-latitude regions.

The results, presented here in terms of electron density and TEC variations, show a strong geometric dependance involving the magnetic field inclination and the propagative direction of the tsunami. If the strongest electron density and TEC perturbations are located around −15°, 0° and 15° North, the structure and amplitude of the modelled perturbation changes in the two studied cases—south–north and north–south tsunami propagation.

Key words: Numerical solutions; Acoustic-gravity waves; Non-linear electromagnetics; Ionosphere/atmosphere interactions; Tsunamis; Early warning.

1 INTRODUCTION

Progress in the detection of ionospheric perturbations has shown that the ionosphere is sensitive to solid Earth phenomena (i.e. earthquake and tsunami). Most of the efforts in the last decade have been made in the detection of the ionospheric signature of surface Rayleigh waves generated by seismic activity. Signatures of these waves have been observed in the plasma velocity using Doppler sounding (Tanaka *et al.* 1984; Artru *et al.* 2004) and over-the-horizon (OTH) radar (Occhipinti 2006) and in the total electron content (TEC) measured by GPS (Calais & Minster 1995, 1996; Calais *et al.* 1998; Ducic *et al.* 2003; Artru *et al.* 2005b; Heki & Ping 2005). For a review of ionospheric seismology based in GPS detection see Lognonné *et al.* (2006).

Normal mode theory applied to the 1-D Earth with a non-isothermal atmosphere, a radiation condition at the top of the model (Lognonné *et al.* 1998) and viscous damping (Artru *et al.* 2001), reproduces the Doppler sounding (Artru *et al.* 2004) and OTH radar (Occhipinti 2006) data with good agreement. However, the interaction between the neutral motion in the atmosphere and the plasma motion in the ionosphere must be modelled for more accurate solution, and so far, the plasma velocity measured at the limit between the *E* and *F* ionospheric layers has been assumed to be the same as the modelled neutral velocity.

This hypothesis is valid at the Doppler and OTH radar sounded altitude (≈150 km), where the neutral–plasma coupling does not strongly depend on magnetic inclination, and the transfer of the velocity from the neutral atmosphere to the ionospheric plasma is near to one-to-one (Kherani *et al.* submitted).

The same hypothesis can't be used in the case of the TEC measured by GPS, where the plasma density is measured instead of the plasma velocity. Moreover, the integrated nature of TEC depends on the entire structure of the ionosphere and does not constrain the local perturbations. The effect of the magnetic field in the observed

perturbation becomes large due to the neutral–plasma coupling complexity in the *F* region.

Concerning tsunami, significant hopes were placed in space remote sensing techniques, especially with the first space altimetry observation of the tsunami in the open sea (Okal *et al.* 1999) and the encouraging work of Artru *et al.* (2005a) on the detection of tsunami signature in the ionospheric TEC. The latter work has opened new perspectives in offshore tsunami detection by ionospheric sounding, anticipated in the past by Peltier & Hines (1976). In essence, Artru *et al.* (2005a) show the TEC perturbation measured by the Japan GPS dense network (GEONET) appeared 22 hours after the peruvian tsunamigenic quake on June 23rd, 2001 ($M = 8.4$ at 20:33 UT). The observed ionospheric travelling wave reaches the Japanese coast with an azimuth and arrival time consistent with tsunami propagation. Moreover, a period between 22 and 33 min, consistent with the tsunami, was identified in the observed TEC signals. The tsunami generated internal gravity waves (IGWs) were, however, superimposed by other signals associated with travelling ionospheric disturbances (TIDs) (Balthazor & Moffett 1997; Aframovich *et al.* 2003). The ionospheric noise is large in the gravity domain (Garcia *et al.* 2005), so the identification of the tsunami signature in the TEC requires quantitative modelling.

The giant tsunami following the Sumatra–Andaman event [$M_w = 9.3$, 0:58:50 UT, 2004 December 26, (Lay *et al.* 2005)], an order of magnitude larger than the Peruvian tsunami, provided worldwide remote sensing observations in the ionosphere, giving the opportunity to explore ionospheric tsunami detection with a vast data set. In addition to seismic waves detected by global seismic networks (Park *et al.* 2005), coseismic displacement measured by GPS (Vigny *et al.* 2005), oceanic sea surface variations measured by altimetry (Smith *et al.* 2005), detection of magnetic anomaly (Iyemori *et al.* 2005; Balasis & Mandea 2007) and acoustic-gravity waves (Le Pichon *et al.* 2005), a series of ionospheric disturbances, observed with different techniques, have been reported in the recent literature (DasGupta *et al.* 2006; Liu *et al.* 2006a,b; Lognonné *et al.* 2006; Occhipinti *et al.* 2006). Two ionospheric anomalies in the plasma velocities were detected north of the epicentre by a Doppler sounding network in Taiwan (Liu *et al.* 2006a). The first was triggered by the vertical displacement induced by Rayleigh waves. The second, arriving one hour later with a longer period, is interpreted by Liu *et al.* (2006a) as the response of ionospheric plasma to the atmospheric gravity waves generated at the epicentre.

A similarly long period perturbation, with an amplitude of 4 TECU[1] peak-to-peak, was observed by GPS stations located on the coast of India (DasGupta *et al.* 2006). These perturbations could be the ionospheric signature of IGWs coupled at sea level with the tsunami. Comparable TEC observations were done for five GPS stations (twelve station-satellite couples) scattered in the Indian Ocean (Liu *et al.* 2006b). The 30 s differential amplitudes are equal to or smaller than 0.4 TECU (which generates amplitudes comparable to the DasGupta *et al.* (2006) observations for periods of ≈165 min, i.e. 30 points) and the arrival times are coherent with the tsunami propagation. The observed satellites were located approximately at the station zenith.

Close to these observations, the Topex/Poseidon and Jason-1 satellites acquired the key observations of the Sumatra tsunami with altimetry profiles. The measured sea level displacement is well explained by tsunami propagation models with realistic bathymetry and provides useful constraints on source mechanism inversions (e.g. Song *et al.* 2005). In addition, the inferred TEC data, required to remove the ionospheric effects from the altimetric measurements (Bilitza *et al.* 1996), showed strong anomalies in the integrated electron density. The modelling proved that the observed anomalies are induced by the tsunami through its propagation in the ocean, neutral atmosphere and plasma (Occhipinti *et al.* 2006).

In this paper, the modelled coupling mechanism between tsunami, neutral atmosphere and plasma, briefly presented by Occhipinti *et al.* (2006), is described in detail with attention paid to the role of Earth's magnetic field. The tsunamigenic electron density anomaly depends on the geomagnetic latitude and is computed here on the global scale to emphasize the consequent heterogeneity. This description helps to define the geographical latitude where the perturbation is strongly visible.

The full theoretical description of the ocean–atmosphere–ionosphere coupling is presented in two steps—the tsunami-atmosphere coupling will be treated in section 2, and the neutral–plasma coupling will be described in Section 3. For more details about the tsunami propagation modelling in the ocean, see Hébert *et al.* (2007).

2 TSUNAMI–ATMOSPHERE COUPLING

Tsunamis are long period oceanic gravity waves (Satake 2002)—their frequency is generally much smaller than the atmosheric Brünt-Vaïsalla frequency and, in the limit of linear analysis, they generate internal gravity waves in the overlying atmosphere (Hines 1972; Lognonné *et al.* 1998). In other words, the coupling mechanism does not transfer a significant propagating energy in the acoustic domain. As a consequence of this theoretical hypothesis and the slow propagation velocity of IGW, a Bussinesq approximation, equivalent to incompressible fluid (Spiegel & Veronis 1960), can be used in the ocean–atmosphere coupling mechanism and tsunami-IGW propagation.

Under these hypotheses, the response of a non-dispersive and non-isothermal atmosphere to the velocity variation induced by ocean vertical displacement, can be described using 3-D Eulerian equations for irrotational and inviscid flow (Nappo 2002):

$$\frac{\partial u_{x1}}{\partial t} + u_{x0}\frac{\partial u_{x1}}{\partial x} + u_{y0}\frac{\partial u_{x1}}{\partial y} + u_{z1}\frac{\partial u_{x0}}{\partial z} = -\frac{1}{\rho_0}\frac{\partial P_1}{\partial x}, \tag{1}$$

$$\frac{\partial u_{y1}}{\partial t} + u_{x0}\frac{\partial u_{y1}}{\partial x} + u_{y0}\frac{\partial u_{y1}}{\partial y} + u_{z1}\frac{\partial u_{y0}}{\partial z} = -\frac{1}{\rho_0}\frac{\partial P_1}{\partial y}, \tag{2}$$

$$\frac{\partial u_{z1}}{\partial t} + u_{x0}\frac{\partial u_{z1}}{\partial x} + u_{y0}\frac{\partial u_{z1}}{\partial y} = -\frac{1}{\rho_0}\frac{\partial P_1}{\partial z} - \frac{\rho_1}{\rho_0}g, \tag{3}$$

$$\frac{\partial u_{x1}}{\partial x} + \frac{\partial u_{y1}}{\partial y} + \frac{\partial u_{z1}}{\partial z} = 0, \tag{4}$$

$$\frac{\partial \rho_1}{\partial t} + u_{x0}\frac{\partial \rho_1}{\partial x} + u_{y0}\frac{\partial \rho_1}{\partial y} + u_{z1}\frac{\partial \rho_0}{\partial z} = 0. \tag{5}$$

The three components of the velocity vector u_x, u_y, u_z, the pressure P and neutral density ρ are the variables taken in our problem. Following the perturbation theory (e.g. Landau & Lifšitc 1975), each involved variable (u_x, u_y, u_z, P, ρ) is broken up in the form $q(x, y, z, t) = q_0(z) + q_1(x, y, z, t)$, where $q_0(z)$ is the unperturbed term with horizontal stratification and $q_1(x, y, z, t)$ is the perturbed term, small on the unperturbed basic state. Here the equations are

[1] The TEC is expressed in TEC units (TECU); 1 TECU = 10^{16} e^- m^{-2}.

linearized at the first-order perturbation.[2] Eqs (1)–(3) are the three components of the Navier–Stokes equation in the adiabatic case neglecting Earth's rotation, and (4) is the analytical expression of the incompressible hypothesis. The last one (5), is the continuity equation. In the showed equations g is the z-component of gravity acceleration, considered unperturbed in the cowling hypothesis (Cowling 1941), and depending only on z; u_{x0} and u_{y0} are the two components of horizontal background winds. The vertical background wind u_{z0} is neglected, as it is generally much smaller than the horizontal ones. All the unperturbed parameters describing the neutral atmosphere (nominally ρ_0, showed in Fig. A1, u_{x0} and u_{y0}) are obtained from the empirical model NRLMSISE-00 (Picone *et al.* 2002).

In this paper, we neglect the curvature of the Earth, and therefore, all equations are expressed in a Cartesian 3-D frame where $\hat{x}$, $\hat{y}$ and $\hat{z}$ are eastwards, northwards and upwards, respectively. Only the vertical velocity of sea surface displacement generates atmospheric disturbances when the interface between the ocean and atmosphere is assumed to be flat and without a boundary layer (Hines 1972; Peltier & Hines 1976). By a Fourier transformation in 2-D (x, y) and time (t), we decompose the perturbation fields in plane waves with horizontal wavenumbers k_x, k_y and wave angular frequency ω; consequently, the variables stated above are rewritten in the form

$$\begin{aligned} u_{j1}(x,y,z,t) &= \tilde{u}_j(z)e^{i(k_x x+k_y y-\omega t)},\\ &\text{where } j = x, y, z,\\ \rho_1(x,y,z,t) &= \tilde{\rho}(z)e^{i(k_x x+k_y y-\omega t)},\\ P_1(x,y,z,t) &= \tilde{P}(z)e^{i(k_x x+k_y y-\omega t)}. \end{aligned}$$

In the frequency domain, eqs (1)–(5) can be expressed through the vertical propagator $\frac{\mathrm{d}V}{\mathrm{d}z} = A\cdot V$ explicitly described by the following vector V and matrix A:

$$V = \begin{pmatrix} \tilde{u}_z^* \\ \tilde{P}^* \end{pmatrix},$$

$$A = \begin{bmatrix} -\frac{1}{\Omega}\left(k_x \frac{\mathrm{d}u_{x0}}{\mathrm{d}z} + k_y \frac{\mathrm{d}u_{y0}}{\mathrm{d}z}\right) & \frac{1}{2}\frac{\mathrm{d}\ln\rho_0}{\mathrm{d}z} - \frac{i(k_x^2+k_y^2)}{\Omega} \\ i\left(\Omega + \frac{g}{\Omega}\frac{\mathrm{d}\ln\rho_0}{\mathrm{d}z}\right) & -\frac{1}{2}\frac{\mathrm{d}\ln\rho_0}{\mathrm{d}z} \end{bmatrix}.$$

Here, $\tilde{u}_z^* = \sqrt{\rho_0}\tilde{u}_z$ and $\tilde{P}^* = \frac{\tilde{P}}{\sqrt{\rho_0}}$ are the renormalized vertical velocity and pressure. The former is homogeneous to the square-root of energy—during the vertical propagation both variables are free of the exponential amplification induced by vertical decrease of density ρ_0. $\Omega = \omega - u_{x0}k_x - u_{y0}k_y$ is the intrinsic frequency relative to the flow induced by the horizontal wind (Nappo 2002). As we are focusing on the role of geomagnetic field, the effect of the winds in the IGW propagation is not emphasized in this paper, but it can theoretically introduce a partial enlargement of the IGW amplitude during the propagation against the wind (Sun *et al.* 2007).

The propagation of the tsunami signal in the atmosphere starts at the ocean–atmosphere surface and the boundary condition is expressed by the continuity of vertical displacement; in other words $\tilde{u}_z$, injected in the vertical propagator, is the 3-D Fourier transform of the velocity field $u_z(x,y,t)$ induced by the tsunami at sea surface. The initial condition for pressure $\tilde{P}^*$ is obtained from the propagator using a total spectral analysis in four dimensions (x, y, z, t). The value of k_z is known at the ocean–atmosphere interface ($z = 0$). Consequently, $\tilde{P}^*$ depends here on $\tilde{u}_z^*$, the angular frequency ω, the neutral density background ρ_0 and the three wavelengths k_x, k_y, and k_z:

$$\tilde{P}^* = \frac{i}{\left(k_x^2+k_y^2\right)}\left(k_x\frac{\mathrm{d}u_{x0}}{\mathrm{d}z} + k_y\frac{\mathrm{d}u_{y0}}{\mathrm{d}z} + \Omega k_z + -\frac{1}{2}\Omega\frac{\mathrm{d}\ln\rho_0}{\mathrm{d}z}\right)\tilde{u}_z^*,$$

where

$$\begin{aligned} k_z &= \sqrt{k_z^2} \quad \text{if} \quad k_z^2 \geq 0,\\ k_z &= i\sqrt{-k_z^2} \quad \text{if} \quad k_z^2 \leq 0, \end{aligned} \tag{6}$$

and

$$k_z^2 = \left(k_x^2+k_y^2\right)\left(\frac{N^2}{\omega^2}-1\right) - \left(\frac{N^2}{2g}\right)^2,$$

where $N^2 = -g\frac{\mathrm{d}\ln\rho_0}{\mathrm{d}z}$ is the Brünt-Vaı ssala frequency.

Only the contribution corresponding to the spectrum portion with real k_z values (eq. 6) is taken into account in the propagation. The evanescent waves, the reflected downwards waves and the effect of the IGW to the tsunami itself are neglected in this work in accordance with previous works (Peltier & Hines 1976).

As show in Fig. 1, the filtering produced by the k_z selection loses less than 10 per cent of the energy contained in the tsunami signal. The power spectrum computed along ω for each couple (k_x, k_y) shows that only the high frequency noise is trapped in the atmospheric filtering induced by the propagator. Similar results for IGW propagation from the surface to 300 km of altitude have been recently obtained by Sun *et al.* (2007) with an equivalent pseudospectral propagator including viscosity and thermal conductivity.

Modes resulting from our propagator, for a given period T and horizontal wavelength $\lambda_h = \sqrt{\lambda_x^2+\lambda_y^2}$, are shown in Fig. 2 for horizontal velocity $u_h = \sqrt{u_x^2+u_y^2}$, vertical velocity u_z, pressure P_1 and density ρ_1. The numerical non-isothermal modes are compared with the analytical solution obtained for an isothermal atmosphere. We observe in the non-isothermal modes the presence of the thermopause, located at about 125 km, where the isothermal hypothesis ceases to be valid.

Below the thermopause, most of the energy is concentrated in the density, pressure and horizontal velocity fields; above the thermopause, the energy migrates from pressure, density and horizontal velocity modes to the vertical velocity mode—its amplitude increases by about 50 per cent. The increase in wavelength with altitude is an expected effect of non-isothermal atmosphere. We recall in the Appendix A the isothermal case, used as a benchmark to validate the numerical solution.

The bathymetry, for a given period T, imposes the horizontal wavelength λ_h of the tsunami as the latter depends on the depth of the ocean H_{water} [$\lambda_h = T\sqrt{gH_{\text{water}}}$ (Satake 2002)]. Therefore, it also affects the vertical propagation of the tsunami-IGW. The mode dependance of oceanic depths H_{water}, for a tsunami wave with a fixed period of 10 min, is shown in Fig. 2. The group velocity can also be computed, as well as the traveltime necessary for reaching 300 km of altitude, the typical location of the maximum of ionization. Note that the ionosphere is reached earlier when the tsunami wave is offshore than when it is propagating through shallow water, near the coast (Fig. 3).

A complete 3-D modelling is shown in Fig. 4 for a simple case of a cylindrical tsunami wave generated by a point source with a dominant wavelength of 180 km and period of 15 min. The consequent horizontal phase/group velocity is 200 m s^{-1} corresponding

[2] The validity of linear theory in the propagation of IGWs in the neutral atmosphere is discussed by Dörnbrack & Nappo (1997).

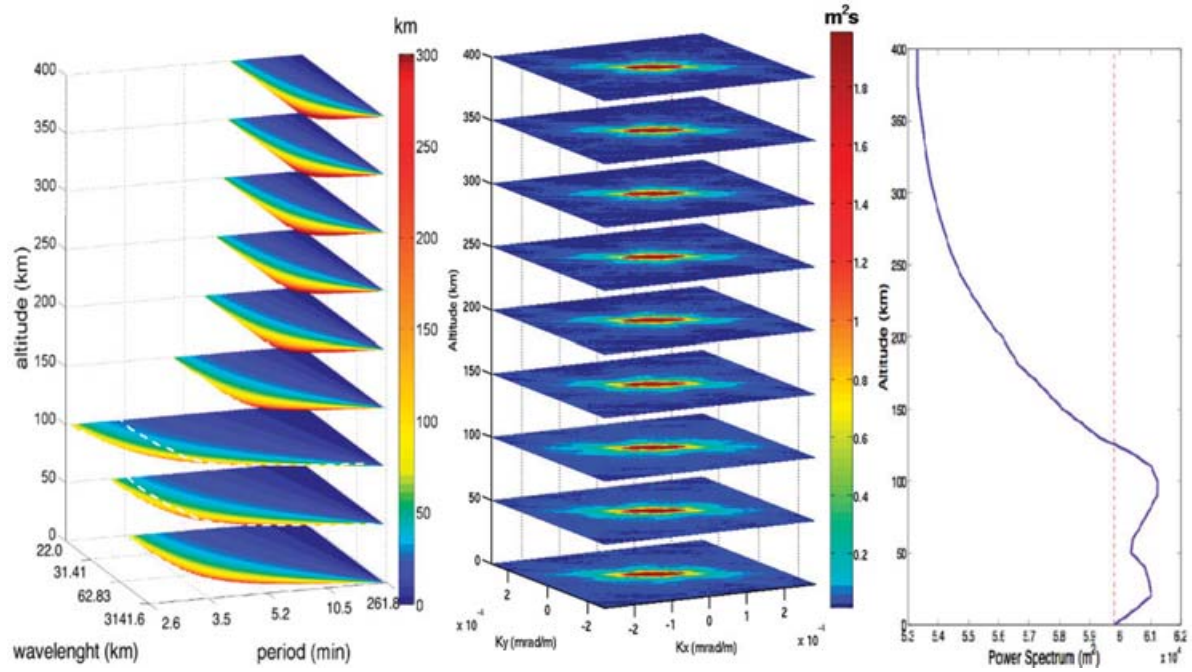

Figure 1. Spectral analysis of the Sumatra tsunami used here as a benchmark to test the filtering effect induced by the numerical propagator. On the left-hand panel: vertical wavelength $\lambda_z = \frac{2\pi}{k_z}$, where k_z is solution of eq. (6). The white dotted line shows the limit of the transferred energy from the ocean into the atmosphere. Central panel: power spectrum computed along ω for each couple (k_x, k_y). The colour scale is saturated to emphasize the noise level, indeed the maximum value of the ω power spectrum is $\approx$90 m^2 s. The vertical propagation preserves the tsunami energy losing only the high frequency noise. Right-hand panel: total power spectrum (m^2) of the tsunami signal. During the propagation less than 10 per cent of the transmitted energy is lost by the filter effect. The red outline marks the initial energy transmitted in the atmosphere. The red outline emphasizes that before the thermopause ($\approx$125 km) the isothermal hypothesis is acceptable, and at this altitude part of the transmitted energy is reflected for the first time.

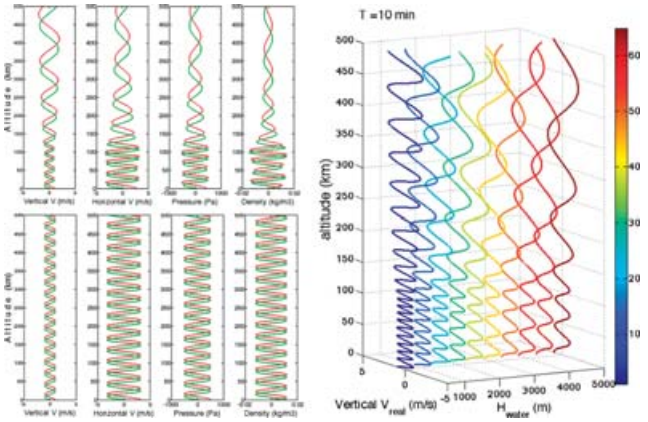

Figure 2. Left-hand panel: Vertical and horizontal components of the velocity, the density and the pressure modes computed by the described vertical propagator with a non-isothermal atmosphere (top). The analytical solution modes for isothermal atmosphere are shown on the bottom figure. The real (red) and imaginary (green) components are shown. The period and horizontal wavelength are 10 min and 94 km, respectively. Right-hand panel: The real component of non-isothermal modes (vertical component of the velocity) with a period of 10 min and different horizontal wavelengths (colour scale in km). The dependence on the ocean deep H_{water} is emphasize. All the modes showed here are normalized to be free of the effect of the exponential amplification induced by vertical decrease of density ρ_0.

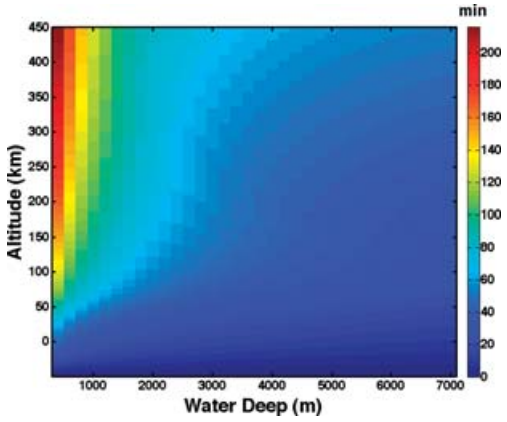

Figure 3. Propagation time of IGWs in the atmosphere generated by an oceanic tsunami with a characteristic period of 10 min. The time variation along the abscissa, put in evidence the bathymetry effect: The atmospheric upward propagation is faster when the tsunami is offshore.

to a tsunami propagating in about 4100 m of water depth. The inversion of the velocity with altitude (wind shear), typical of IGWs structure (Schunk & Nagy 2000), is highlighted by the vertical cross-section. This simple example clearly shows the upward propagation of tsunamigenic IGWs and the time to reach 100 km of altitude where the IGW starts to interact with the ionosphere ($\approx$30 min for the assumed frequency and wavelength). The right-hand side of Fig. 2 shows the wavelength variation during the upward propagation, and the consequent propagation time to reach the ionosphere is shown in Fig. 3. Note that propagation time depends not only on the tsunami period but also on the ocean depth. Indeed, signals in the ionosphere have been observed just 15 min after the tsunami generation in the case of Sumatra event (Occhipinti 2006). In Fig. 5

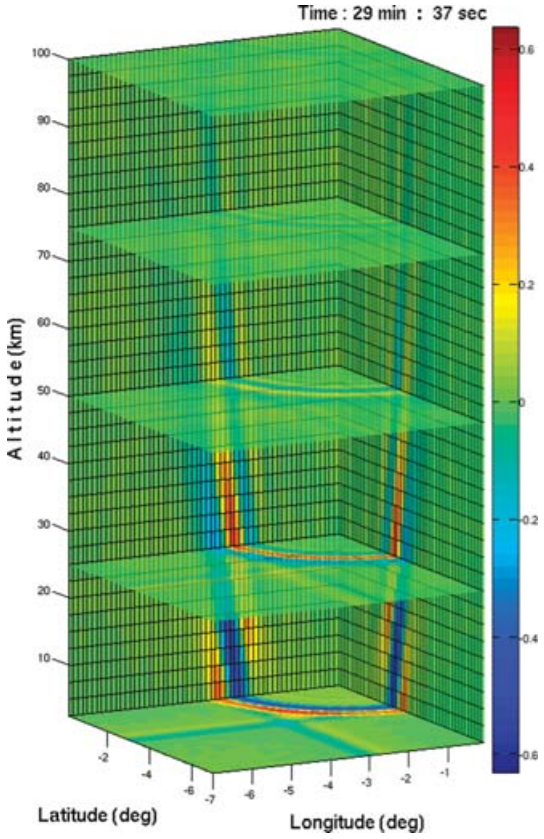

Figure 4. Vertical component of atmospheric normalized velocity ($v\sqrt{\rho_0}$, $[\mathrm{m\,s^{-1}}\sqrt{\mathrm{kg\,m^{-3}}}]$) perturbed by tsunamigenic IGWs for a simple cylindrical wave case. Inversions of velocity with altitude (wind shear) typical of IGWs are clearly shown in the vertical cross-section.

(and movie S1 see the Supplementary Material in the online journal) a 2-D IGW modelling induced by a simple tsunami propagation in the global scale is shown. For a more realistic case, e.g. the Sumatra tsunami, see Occhipinti *et al.* (2006).

3 NEUTRAL–PLASMA COUPLING

The propagation of IGW in the neutral atmosphere is known to produce irregularities in the ionospheric plasma (i.e. TIDs), and some studies of the nature of this connection have been made in the past using different assumptions. The first theoretical remarks presented by Hines (1960) proposed the link between IGWs, propagating in the neutral atmosphere, and TIDs, observed in the ionospheric plasma. The following quantitative works (Hooke 1968) started to take into account and analysing the effect of the specific geometry of the measured TEC in the TID observations (Georges & Hooke 1970; Davis 1973).

Recently, TIDs have been extensively modelled (Balthazor & Moffett 1997; Huang *et al.* 1998) to explain the improved observations (Ogawa *et al.* 2002; Saito *et al.* 2002), but, excluding Peltier & Hines (1976) and Occhipinti *et al.* (2006), no theoretical work analysed the effect of tsunamigenic IGWs on the ionospheric plasma. To perform the plasma perturbation produced by the effect of tsunamis, we use a dynamic 3-D ionospheric model (Kherani *et al.* 2004, 2005) under the effect of tsunamigenic IGWs described in the previous section.

We solve the hydromagnetic eqs (7) and (8) (Kelley 1989) for the three principal ions i present in the ionospheric plasma (O_2^+, NO^+ and O^+ for $i = 1, 2, 3$, respectively) and under the effect of the neutral velocity $\vec{v}_n$ perturbation produced by the IGW propagation. The induced plasma velocity v_i for each ion i is taken equal to zero in the unperturbed state. The induced ion pressure and ion density are p_i and ρ_i, respectively. The initial density distributions of the three ion species and the electrons, as well as the collision frequency between neutral and ion, μ_{in}, are shown in Fig. A2. The electric, magnetic and gravity fields are $\vec{E}$, $\vec{B}$ and $\vec{g}$, respectively.

The associated equations can be written as:

$$\frac{\partial n_i}{\partial t} + \nabla \cdot (n_i \vec{v}_i) = \pm\beta n_i - \alpha n_i^2, \tag{7}$$

$$\rho_i \frac{d\vec{v}_i}{dt} = -\nabla p_i + \rho_i \vec{g} + n_i q_i \left(\vec{E} + \vec{v}_i \times \vec{B}\right) - \rho_i \mu_{\mathrm{in}} \left(\vec{v}_i - \vec{v}_n\right), \tag{8}$$

$$n_e = \sum_{i=1}^{3} n_i. \tag{9}$$

The terms in the right-hand side of continuity eq. (7) correspond to the chemical ion loss by the charge exchange process (β) and the dissociative recombination (α) process. As shown by Occhipinti *et al.* (2006), these effects do not play a primary role in the amplitude of the ionospheric signature of a tsunami-IGW. However, this is fully taken into account because of the critical role they play in the ion equilibrium and the long term evolution of the plasma density after being perturbed by the tsunami-IGWs. The explicit chemical reactions taken into account are:

$$\begin{aligned} O_2^+ + e^- &\xrightarrow{\alpha} O + O, \\ NO^+ + e^- &\xrightarrow{\alpha} N + O, \\ O^+ + O_2 &\xrightarrow{\beta} O_2^+ + O, \\ O^+ + NO &\xrightarrow{\beta} NO^+ + O. \end{aligned}$$

Here α is taken into account only for molecular ions, and β has a sign consistent with density increasing for molecular ions (O_2^+, NO^+) and decreasing for atomic ion (O^+). The acceleration term in the momentum equation (eq. 8) can be neglected for gravity wave propagation (Hooke 1968; Davis 1973) as the frequency is much smaller that the magnetic gyro-frequency $\Omega_i = qn_iB/\rho_i$. This approximation supplies the linear dependence between the ion velocity $\vec{v}_i$ and neutral velocity $\vec{v}_n$:

$$v_{i\parallel} = v_{n\parallel} - \frac{K_{i\parallel}}{\rho_i \mu_{\mathrm{in}}}, \tag{10}$$

$$v_{i\odot} = v_{n\odot} + \frac{\Omega_i}{\mu_{\mathrm{in}}} v_{i\perp} + \frac{K_{i\odot}}{\rho_i \mu_{\mathrm{in}}}, \tag{11}$$

$$v_{i\perp} = v_{n\perp} - \frac{\Omega_i}{\mu_{\mathrm{in}}} v_{i\odot} + \frac{K_{i\perp}}{\rho_i \mu_{\mathrm{in}}}, \tag{12}$$

where ($K_{i\parallel}, K_{i\odot}, K_{i\perp}$) are the three components of the forcing term $\vec{K}$ independent of the magnetic field:

$$\vec{K} = -\nabla p_i + \rho_i \vec{g} + n_i q_i \vec{E}.$$

The indexes denote the parallel $\parallel$ and perpendicular ($\odot$, $\perp$) components to the magnetic field $\vec{B} = (B, 0, 0)$ in a direct vector basis.

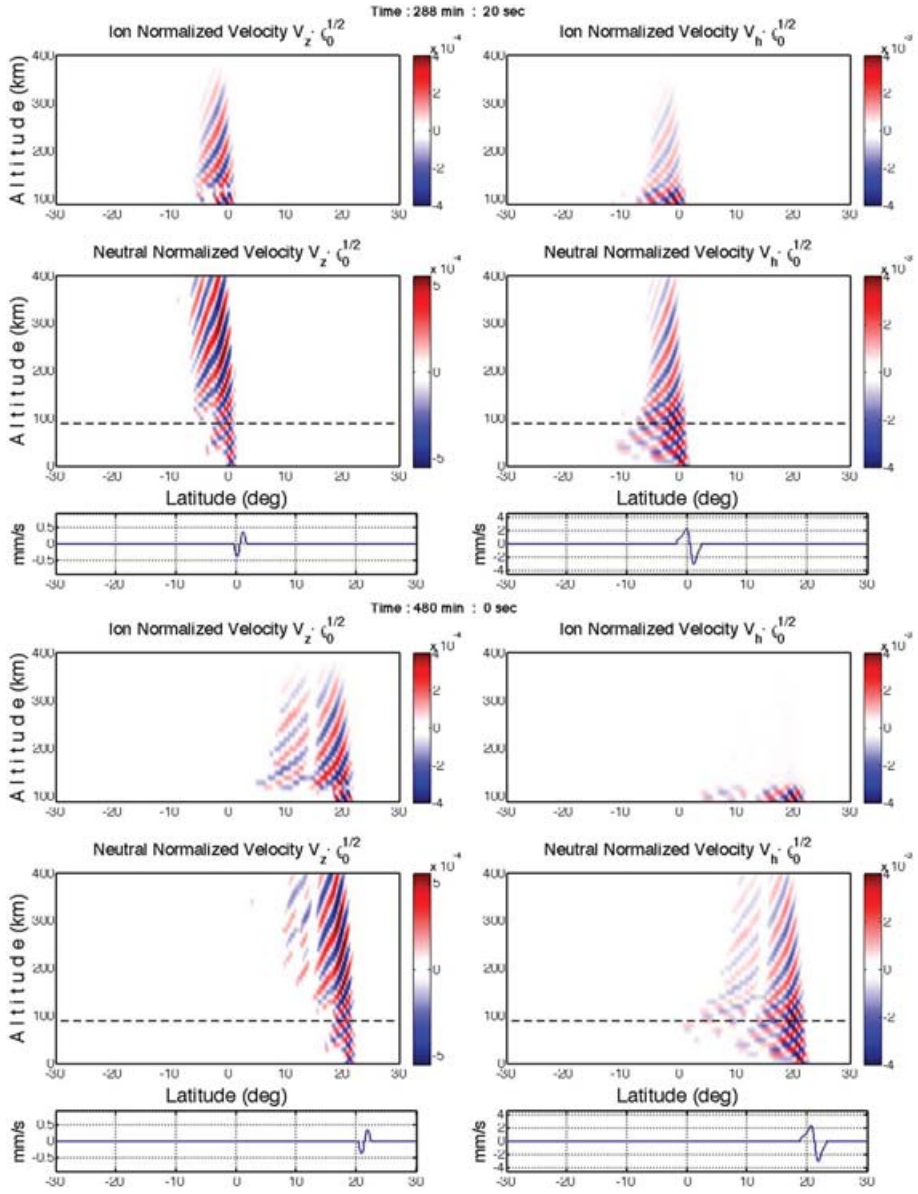

Figure 5. Neutral and ion normalized velocity ($v\sqrt{\rho_0}$, $[\mathrm{m\,s^{-1}}\sqrt{\mathrm{kg\,m^{-3}}}]$) induced by tsunamigenic IGW propagation at 288 min : 20 s (top panel) and 480 min (bottom panel). The shown plasma velocity is the sum of the velocities of the three ion species O^+, O_2^+ and NO^+. The plasma model starts at 90 km and its limit is highlighted in the neutral plot by the dotted black line. The blue lines in the small plots show the vertical (left-hand part) and horizontal (right-hand part) velocity perturbation at the sea level produced by the tsunami. The characteristic period of the simulated tsunami is ≈20 min and its horizontal wavelength ≈230 km. Clearly evident is the dependence of magnetic inclination ($I = [-40^\circ : 20^\circ]$, with $I = 0^\circ$ close to 10°N, see Fig. A3) in the horizontal component of ion velocity. The complete movie is included in Supplementary Materials (see movie S1).

We observe that only the perpendicular components of the ion velocity are affected by the magnetic field by the way of the magnetic gyro-frequency $\Omega_i = qn_iB/\rho_i$. To understand the nature of ion velocity induced by the tsunamigenic IGWs, an example is shown in the Fig. 5 in two time steps. The shown vertical and horizontal components of the velocity are derived from eqs (10) to (12) by considering a simple tsunami (wave package with a principal period of 20 min and wavelength of 230 km) moving in the northward direction. Note that the momentum transfer is maximum in horizontal direction near the geomagnetic equator while it is maximum in vertical direction far way from the equator. This indicates that the IGW velocity component parallel to the geomagnetic field is very important for significant coupling with the ionosphere. This effect increases with altitude as the ratio Ω_i/μ_i increases. Thus, in the E region, this effect is minimum and coupling is mainly dictated by the IGW amplitude. The effect of the geomagnetic field increases with altitude and the IGW component parallel to field lines becomes important for the coupling in the F region. We also note that the coupling does not increases indefinitely, since at higher altitude, the collision frequency becomes very small, leading to the inefficient communication between IGWs and ionospheric plasma. Also, the ionospheric density and IGWs amplitude becomes small at higher altitudes, which further reduces the coupling.

Since the momentum transfer in the E region is unaffected by the magnetic field inclination, unlike in the F region, the amplitude of ion velocity v_i reflects the neutral velocity v_n. This result

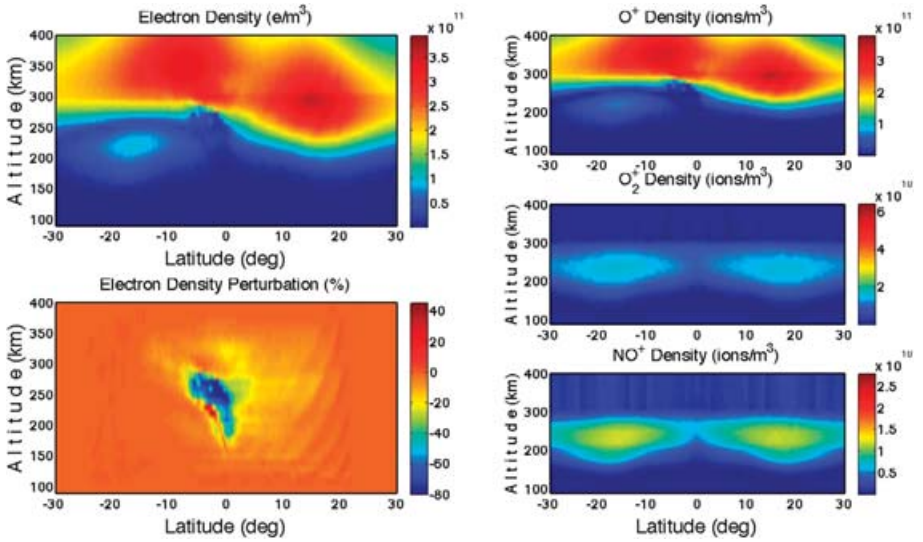

Figure 6. Ionospheric model under the effect of neutral motion produced by tsunami-generated IGWs shown in the Fig. 5 at 480 min. The ionospheric electron density and its variation from the unperturbed model are shown on the top left-hand panel and bottom left-hand panel, respectively. On the right-hand side, O^+, O_2^+ and NO^+ ion densities are shown from top to bottom. The complete ionospheric model evolution under the effect of IGWs is showed in the Supplementary Material (see movie S2).

confirms the one-to-one correspondence observed by Doppler sounding (Artru *et al.* 2004) and OTH radar (Occhipinti 2006).

In the next step, the ion densities n_i for the three species are obtained using the computed ion velocities $\vec{v}_i$ and solving the non-linear continuity eq. (7) by a space–time finite-differences solver (Kherani *et al.* 2005). The electron density n_e is extrapolated from ion densities n_i using the hypothesis of charge neutrality (9).

Physically, to resume, the neutral atmospheric motion $\vec{v}_n$ induces fluctuations in the plasma velocity $\vec{v}_i$ (Fig. 5). Indeed, changes in the wind direction, produced by the typical structure of IGWs, induce either increasing and decreasing of plasma density forming layers in the ionosphere by wind-shear mechanism (Fig. 6). This mechanism is also known to be responsible for the sporadic *E* and mid-latitude layers inducing local electron density variations higher than 80 per cent of the local value (Schunk & Nagy 2000). The momentum transfer from $\vec{v}_n$ to $\vec{v}_i$ is primarily dominated by the frictional term driven by collision frequency $\mu_{\rm in}$ and by the Lorentz term associated with the Earth magnetic and electric field ($\vec{B}$ and $\vec{E}$). The electric field polarization, under the effect of IGWs, is computed in this modelling but his effect on the resulting perturbation of ion velocities, and ion's and electron's densities is negligible. In contrary to the electric field *E*, the magnetic field *B* is considered unperturbed in this study.

The results of the ionospheric simulation shown in Fig. 5 are presented in terms of ion and electron density variations in Fig. 6. In accordance with the ionosphere composition, we observe that the atomic ion O^+ is more perturbed than the molecular ions NO^+ and O_2^+. Indeed, O^+ is the most common ion in the *F* region, where the tsunami signature is prominently observed.

Both Table 1 and Fig. 7 resume the N_e perturbation induced by the IGW neutral motion in the equator and mid-latitudes. Here the N_e perturbations produced by the horizontal and vertical components of IGW have been computed separately for academic purposes. We deduce that the plasma density variations in the high ionosphere are mainly driven by the horizontal component of IGW; the effect of this, as previously discussed, reaches a maximum when it is parallel to the magnetic field.

In the *E* region, the role of the geomagnetic field is less perceptible and the contributions of horizontal and vertical components of the IGW are comparable. We deduce the weak *B* dependence of the vertical component of the IGW: no differences are observed between the *E* and *F* regions, as well as between the equatorial and mid-latitude regions. A north–south dichotomy appears, driven by the northward tsunami propagation.

To explore this dichotomy, the southward tsunami propagation case is presented. In the Northern Hemisphere, the electron density perturbation does not exceed 10 per cent in both *E* and *F* regions; however, when the tsunami travels south of −10°N, the electron density perturbation becomes much larger, reaching amplitudes of 80 per cent of the local density, and then goes to zero when the IGW go over the equatorial anomaly. In addition, the perturbation is located more to the south and closer to the maximum of ionization than in the northward propagation case, implying a stronger perturbation in the TEC (Figs 8 and 9, Table 2).

This effect has been partially observed by Topex/Poseidon and Jason-1 and is described by Occhipinti *et al.* (2006) as a consequence of a complete development of mature IGWs in the neutral atmosphere. Here, we conclude that this effect is a consequence of the magnetic field and we emphasize the role of the propagation direction and geometric structure of the tsunami in the ionospheric response.

In Fig. 9, the described case for the northward and southward tsunami propagations are shown in terms of TEC perturbations. In both cases, the modelling shows TEC perturbations in order of a fraction of TEC-unit (TECU) coherent with the GPS observations (DasGupta *et al.* 2006; Liu *et al.* 2006b; Lognonné *et al.* 2006). In the northward case, the perturbation is negative and amplitude has its first negative peak at the geographic equator and a second decrease in amplitude near the magnetic equator (see Appendix B for magnetic field inclination, Fig. A3).

The southward tsunami propagation shows a different signature in the ionospheric plasma (Fig. 8) and, as described above, the correspondent TEC perturbation appears positive and has a more localized strong amplification than in the northward case (Fig. 9).

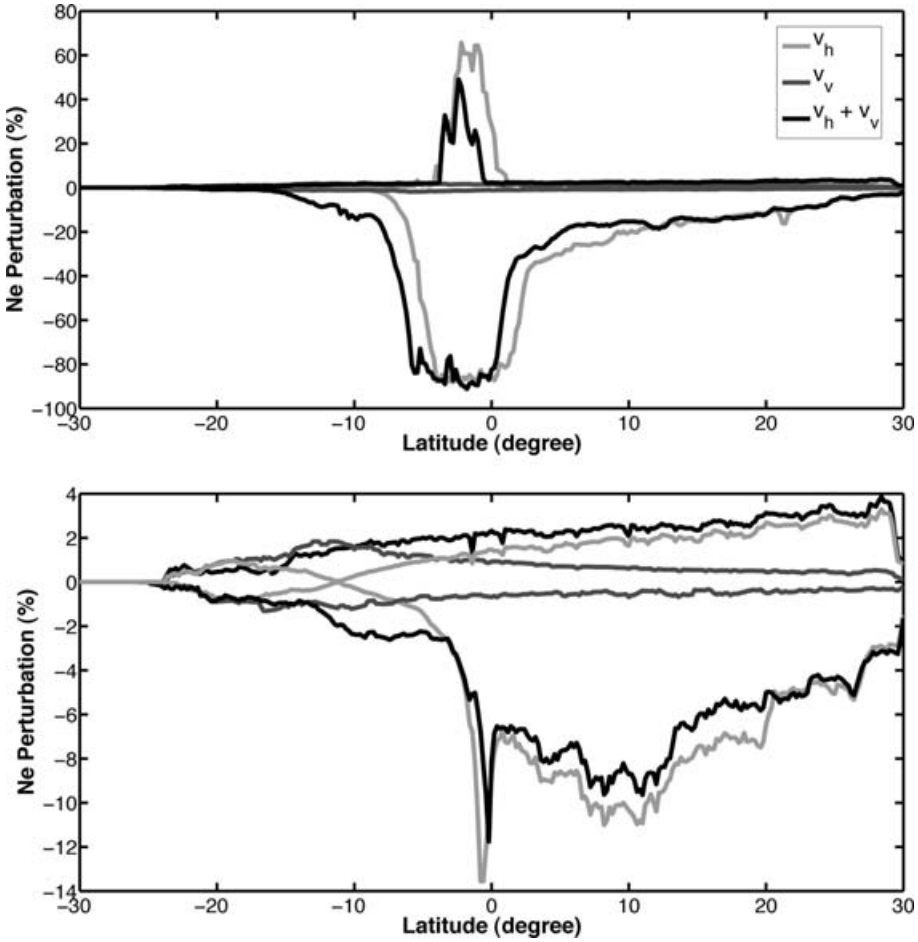

Figure 7. Latitudinal dependance of the local maximal and minimal electron density perturbation in the *F* (top panel) and *E* (bottom panel) regions produced by IGWs coupled with a northward tsunami propagating. The vertical displacement at sea level is in order of 25 cm. The black line shows the realistic response produced by IGWs. The grey lines, show the hypothetical perturbation induced by th only vertical (light-grey) and horizontal (dark-grey) components of IGW velocity. The *F*-region perturbation is strongly dependent on magnetic inclination ($I = [-40^\circ : 20^\circ]$, with $I = 0^\circ$ near 10°N, see Fig. A3); in contrast, in the *E*-region, after the formation of IGWs, the amplitude perturbation is less-dependent of geomagnetic latitude. Each line (i.e. black, light-grey, dark-grey) shows the maximum (above zero) and the minimum (below zero) perturbation.

In this computation, the geometrical dispersion of the tsunami propagation is not taken into account, and the amplitude of vertical displacement at the sea surface is of order 25 cm during the whole propagation, this value is a good estimation of the mean displacement produced by Sumatra tsunami in the Indian Ocean.

The principal direction of the Sumatra tsunami propagation in the India Ocean, near the location of Topex and Jason observations, is South-West; this explain why in the more realistic modelling of Occhipinti *et al.* (2006) appears a strong perturbation in the TEC, similar to ones observed in the southward case, and coherent in latitude location. Unfortunately, the strong TEC perturbation located in the Southern Hemisphere modelled by Occhipinti *et al.* (2006) is only partially observed by Topex/Poseidon and Jason-1: the passages of the two satellites in the zone around $\approx -10^\circ$N of latitude happen only during the formation of the perturbation.

In agreement with the realistic modelling of the Sumatra tsunami by Occhipinti *et al.* (2006), the amplitudes of TEC and electron density perturbations shown here are strongly increased between -20° and 20°N latitude. If the amplitude variations in the electron density perturbations, and consequent TEC, are stronger in a realistic tsunami, this is the effect of the non-linear evolution of the ion densities. The geometrical heterogeneity induced by the tsunami

Table 1. Local density perturbation in the *E* and *F* regions, and vertical TEC (V-TEC) perturbation produced by the propagation of IGW shown in the Fig. 5 for the realistic case $u_z + u_h$ and the two demonstrative cases, u_h and u_z, where only one component of the IGW velocity was used.

	Equatorial region			Mid-latitude		
	u_z (per cent)	u_h (per cent)	$u_z + u_h$ (per cent)	u_z (per cent)	u_h (per cent)	$u_z + u_h$ (per cent)
E-region	−2:2	−2:10	−2:10	−2:2	−2:10	−2:10
F-region	−2:2	−80:60	−80:50	−2:2	−20:2	−20:2
V-TEC			−0.7:0.01 TECU			−0.4:0.01TECU

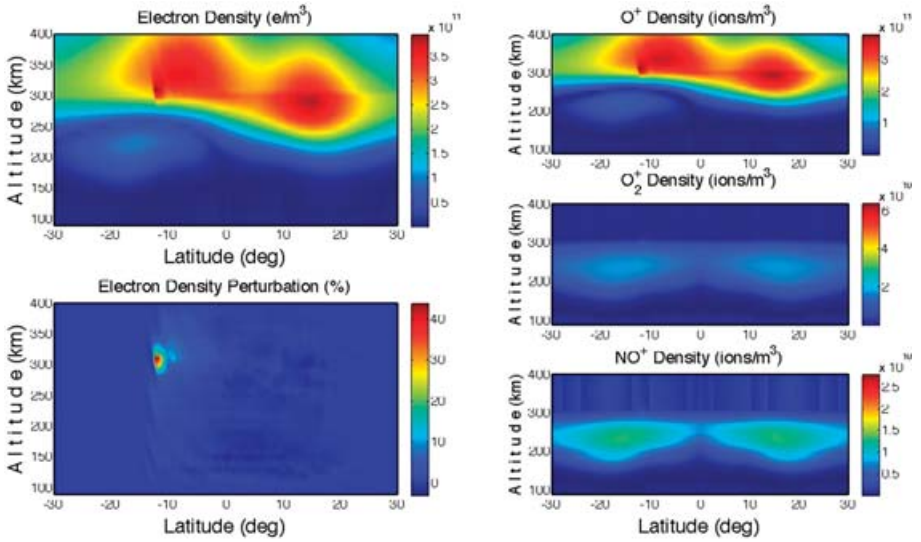

Figure 8. Ionospheric perturbations produced by southward tsunami propagation. As in Fig. 6, the perturbed electron and ions densities are shown in the four panels. We observe a strong perturbation located in the South Hemisphere above 300 km altitude; whereas, for northward tsunami propagation, the maximum perturbation is observed in the equatorial region and below 300 km altitude. The snapshot is taken at 413 min and 20 s. The complete ionospheric model evolution under the effect of southward IGWs is shown in the Supplementary Material (see movie S3).

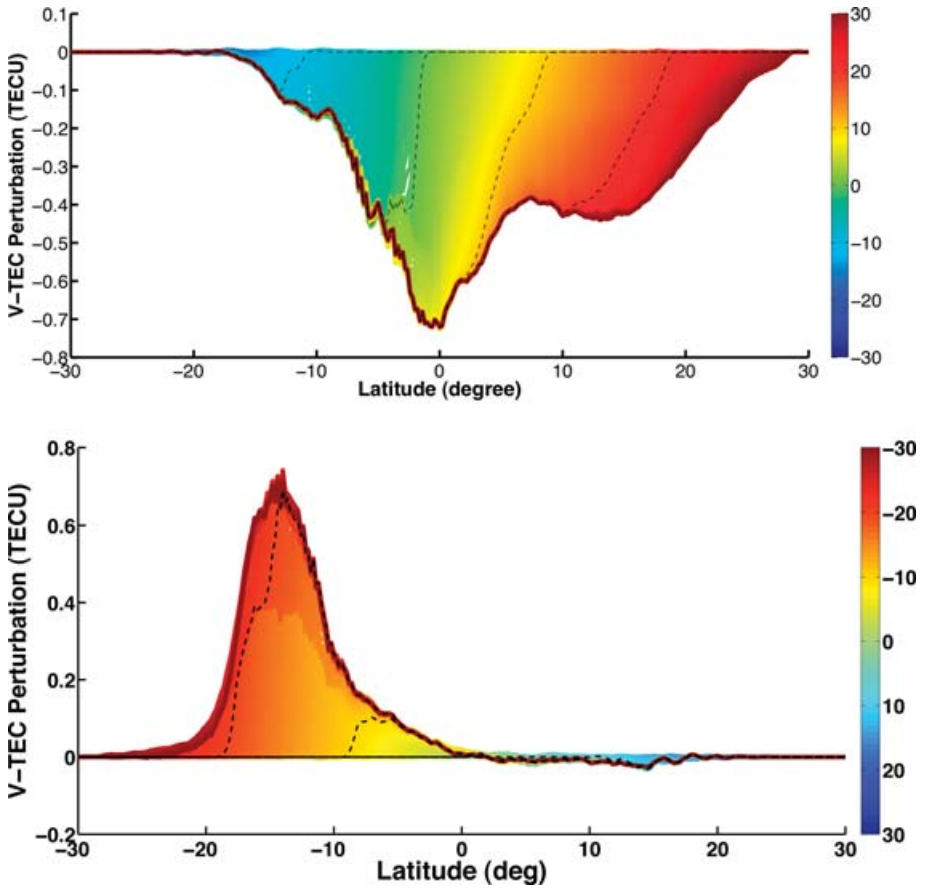

Figure 9. Superimposition of the vertical TEC variation curves. Each one-colour curve shows the vertical TEC variation induced by IGWs coupled at the oceanic surface with a tsunami moving northwards and southwards for the top and bottom panels, respectively. The complete propagation time is 558 min, allowing the tsunami wave front to move from −30°N to 30°N in latitude (northward case) and 30°N to −30°N (southward case). For example, Fig. 5 shows two snapshots of the northward propagation of tsunamigenic IGW at 288 min : 20 s and 480 min. The colours indicate the position of the tsunami wave front at the sea surface during the 558 min of its propagation. The dotted lines show four chosen TEC variation curves produced when the tsunami is located at −10°N, 0°N, 10°N and 20°N of latitude for the northward case and 10°N, 0°N, −10°N and −20°N for the southward case, respectively.

Table 2. Local density perturbation in the *E* and *F* regions, and vertical TEC (V-TEC) perturbation produced by the IGW coupled with the southward tsunami. This table resume Fig. 8 and Fig. 9 (bottom). Contrary to Table 1 only the complete case $u_z + u_h$ is showed here.

	[−20°:−10°] Region $u_z + u_h$ (per cent)	Elsewhere $u_z + u_h$ (per cent)
E-region	−3:3	−3:3
F-region	−20:95	−3:3
V-TEC	−0.004:0.75 TECU	−0.04:0.01 TECU

waveform (Occhipinti *et al.* 2006) adds to the latitude dependence driven by the magnetic field, highlighting the difficulties in the identification of tsunami signature in the ionosphere.

In summary, the sensitivity of modern ionospheric sounders (i.e. GPS, OTH radar, Doppler sounding, backscattered radar, etc.) with the help of the modelling described here can overcome the identification difficulties and be of considerable aid to the classical methods in oceanic monitoring and tsunami warning systems.

4 CONCLUSIONS

The theoretical analysis of the energy exchange between ocean, neutral atmosphere and ionospheric plasma presented here shows that the ionospheric signature produced by a tsunami can be quantitatively calculated. The accurate study of these tsunamigenic phenomena reveals a latitude dependence on the electron density perturbation, driven by the Earth's magnetic field. This heterogeneity is consistent with the observations reported in the recent literature that followed the Sumatra tsunami (Liu *et al.* 2006b; Occhipinti *et al.* 2006). We highlight the facilities in detection of tsunamis via ionospheric sounding in the equatorial zone between 20°S and 20°N due to the parallel configuration between the horizontal component of neutral velocity of tsunamigenic IGWs and the magnetic field. This equatorial zone includes most of the countries on the Indian ocean reached by the Sumatra tsunami (e.g. Indonesia, Sri Lanka, South of India and Thailand). Notwithstanding the heterogeneity in the tsunamigenic response of the ionosphere, the detection at the middle and hight latitudes (after 20°) is possible.

The sensitivity of the TEC measured by GPS can be affected by the high noise level in the gravity frequency domain (<0.1 TECU) (Garcia *et al.* 2005), anyway, the hight density coverage of the GPS stations (e.g. Japan) can help the data analysis looking the coherence of the ionospheric perturbation with the tsunami propagation.

We also note that, in contrast to the perturbed electron density, the tsunamigenic anomaly in the plasma velocity located in the *E*-region is independent of the geomagnetic field. This result shows that the instruments sounding the *E*-region—such as Doppler sounding, OTH radars or incoherent scatter radars—can be useful tools in the tsunami detection by the way of ionospheric sounding in the *E*-region. In particular, our attention is turned to the coverage of OTH radars able to sound large portions of the ionosphere overlooking the tsunamigenic zones (e.g. the OTH radar Nostradamus covering the Mediterranean Sea). In addition, the propagation time that IGWs need to reach the *E*-region is substantially shorter than the time to reach the *F*-region.

Table 3 describes the zones strongly reached by tsunami in the last centuries and proposes useful ionospheric sounding techniques. All technical suggestions are based on existing networks. We also imagine these two technics work together in a joint inversion of ionospheric parameters to reconstruct the entire 3-D perturbation produced in the ionosphere by tsunamis. Dense GPS network have recently been used to perform a ionospheric tomography (Garcia *et al.* 2005) based on the inversion of TEC measurements. Unfortunately, the high frequency of the GPS signals ($L_1 = 1575.42$ MHz and $L_2 = 1227.6$ MHz) only allow the accurate reconstruction of the ionospheric heterogeneity near the maximum of ionization located in the *F*-region around 300 km. The sensitivity of OTH radar to the variations of ionospheric parameters in the *E*-region (Occhipinti 2006) can improve the GPS tomography resolution (Fridman & Nickisch 2001).

These results open new perspectives for future ocean monitoring and improved tsunami warning systems helped by ionospheric sounding using GPS stations as well as OTH radars. Anyway, with a critic constructive optic, we emphasize the limits of the ionospheric sounding in the tsunami detection. First, as showed here, the relationship between the TEC perturbation observed by GPS and the amplitude of the sea surface displacement is not linear. Theoretically, this relationship is linear sounding at the *E*-region by OTH radars but, at the present, only the signature of Rayleigh waves has been observed with this instrument (Occhipinti 2006). Second, the propagation time of acoustic-gravity waves from the sea surface to the ionospheric heights allows the use of the ionospheric monitoring only for tsunami warning confirmation purpose and for following the tsunami propagation on the open sea.

Both of these limits may be reduced by exploring the tsunami–atmophere–ionosphere coupling in more detail. In particular, we emphasize that the presented coupling method, working principally in the gravity domain, accurately reproduces the signature in the ionosphere produced by the tsunami propagation in the open sea. Close to the epicentre of tsunamigenic Earthquakes, where a more complex signal is transfered in the atmosphere (in both, the acoustic and gravity domain) the equations must to be solved without the Businesq approximation in the neutral atmosphere and taking into account the acceleration terms in the momentum equation for plasma

Table 3. Disastrous tsunamis in the last centuries and the ionospheric sounding techniques suggested to improve the tsunami warning system. Note that all the network and instrument proposed already exist and don't need hardware implementations, however, most of them don't operate in real time.

Location	Event	Death toll	Proposed techniques
Indonesia	Sumatra, 2004 December 26	130 736	GPS
Japan	from 1605 to 1933	108 000	GPS dense network
Portugal and Marocco	Lisbon, 1975 November 1	100 000	OTH radar
Italy	Messina, 1908 December 28	70 000 (earthquake and tsunami)	OTH radar
Hawaii	from 1946 to 1968	∼1000	GPS
Sri Lanka	Sumatra, 2004 December 26	35 322	GPS
India	Sumatra, 2004 December 26	12 405	GPS
Thailand	Sumatra, 2004 December 26	5395	GPS
Rest of Indian Ocean	Sumatra, 2004 December 26	309	GPS

ions. These issues highlight the future directions of modelling and data analysis on tsunamigenic ionospheric perturbations to estimate the sea level anomaly and aid in the tsunami warning by the way of ionospheric sounding.

ACKNOWLEDGMENTS

This project is supported by the French ANR under contract CATELL-IONONAMI, by CNES and by the French Ministry of Research. We thank A. De Santis and G. Balasis for their constructive and detailed remarks. We thank NRL for development of SAMI2 software. GO thanks J. Tromp for interesting discussion and suggestions, and J. LaBrecque of NASA's Science Mission Directorate for supporting his fellowship at the California Institute of Technology. This is IPGP contribution 2305.

REFERENCES

Aframovich, E.L., Perevalova, N.P. & Voyeikov, S.V., 2003. Traveling wave packets of total elctron content disturbances as deduced from GPS network data, *J. Atmo. Solar-Terr. Phys.,* **65,** 1245–1262.

Artru, J., Lognonné, P. & Blanc, E., 2001. Normal modes modelling of post-seismic ionospheric oscillations, *Geophys. Res. Lett.,* **28**(4), 697–700.

Artru, J., Farges, T. & Lognonn, P., 2004. Acoustic waves generated from seismic surface waves: propagation properties determined from Doppler sounding and normal-mode modeling, *Geophys. J. Int.,* **158**(3), 1067–1077.

Artru, J., Ducic, V., Kanamori, H., Lognonné, P. & Murakami, M., 2005a. Ionospheric detection of gravity waves induced by tsunamis, *J. geophys. Res.,* **160,** 840–848.

Artru, J., Lognonné, P., Occhipinti, G., Crespon, F., Garcia, R., Jeansou, E. & Murakami, M., 2005b. Tsunamis detection in the ionosphere, *Space Res. Today,* **163**, 23–27.

Balasis, G. & Mandea, M., 2007. Can electromagnetic disturbances related to the recent great earthquakes be detected by satellite magnetometers? (Mechanical and Electromagnetic Phenomena Accompanying Preseismic Deformation: from Laboratory to Geophysical Scale, special issue, eds Eftaxias, K., Chelidze, T. & Sgrigna, V.), *Tectonophysics,* **431,** 1–4, 173–195, doi:10.1016/j.tecto.2006.05.038.

Balthazor, R.L. & Moffett, R.J., 1997. A study of atmospheric gravity waves and travelling ionospheric disturbances at equatorial latitudes, *Ann. Geophysicae,* **15,** 1048–1056.

Bilitza, D., 2001. International Reference Ionosphere 2000, *Radio Sci.,* **36**(2), 261–275.

Bilitza, D., Koblinsky, C., Zia, S., Williamson, R. & Beckley, B., 1996. The equator anomaly region as seen by the TOPEX/Poseidon satellite, *Adv. Space Res.,* **18**(6), 23–32.

Calais, E. & Minster, J.B., 1995. GPS detection of ionospheric perturbations following the January, 1994, Northridge earthquake, *Geophys. Res. Lett.,* **22**(9), 1045–1048.

Calais, E. & Minster, J.B., 1996. GPS detection of ionospheric perturbations following a space shuttle ascent, *Geophys. Res. Lett.,* **23**(15), 1897–1900.

Calais, E., Minster, J.B., Hofton, M.A. & Hedlin, M.A.H., 1998. Ionospheric signature of surface mine blasts from Global Positioning System measurement, *Geophys. J. Int.,* **132,** 191–202.

Cowling, T.G., 1941. The non-radial oscillations of polytropic stars, *Mon. Not. Roy. Astron. Soc.,* **101,** 369–373.

DasGupta, A., Das, A., Hui, D., Bandyopadhyay, K.K. & Sivaraman, M.R., 2006. Ionospheric perturbation observed by the GPS following the December 26th, 2004 Sumatra-Andaman earthquake, *Earth Planet. Space,* **35,** 929–959.

Davis, M.J., 1973. The integrated ionospheric response to internal atmospheric gravity waves, *J. Atmos. Terr. Phys.,* **35,** 929–959.

Dörnbrack, A. & Nappo, C.J., 1997. A note on the application of linear wave theory at a critical level, *Boundary-Layer Meteorol.,* **82,** 399–416.

Ducic, V., Artru, J. & Lognonné, P., 2003. Ionospheric remote sensing of the Denali Earthquake Rayleigh surface waves, *Geophys. Res. Lett.,* **30**(18), 1951, doi:10.1029/2003GL017812.

Fridman, O.V. & Nickisch, L.J., 2001. Generalization of ionospheric tomography on diverse data source: reconstrction of the three-dimensional ionosphere from simultaneous vertical ionograms, backscatter ionograms, and total electron content data, *Radio Sci.,* **36,** 1129–1139.

Garcia, R., Crespon, F., Ducic, V. & Lognonné, P., 2005. 3D Ionospheric tomography of post-seismic perturbations produced by Denali earthquake from GPS data, *Geophys. J. Int.,* **163,** 1049–1064, doi:10.1111/j.1365–246X.2005.02775.x.

Georges, T.M. & Hooke, W.H., 1970. Wave-induced fluctuations in ionospheric electron content: a model indicating some observational biases, *J. geophys. Res.,* **75,** 6295–6308.

Hébert, H., Sladen, A. & Schindelé, F., 2007. The great 2004 Indian Ocean tsunami: numerical modeling of the impact in the Mascarene Islands, *Bull. seism. Soc. Am.,* **97**(1A), S208–S222.

Heki, K. & Ping, J., 2005. Directivity and apparent velocity of the coseismic traveling ionospheric disturbances observed with a dense GPS network, *Earth planet Sci. Lett.,* **236**(3–4, 15), 845–855.

Hines, C.O., 1960. Internal atmospheric gravity waves at ionospheric height, *Can. J. Phys.,* **38,** 1441–1481.

Hines, C.O., 1972. Gravity waves in the atmosphere, *Nature,* **239,** 73–78.

Hooke, W.H., 1968. Ionospheric irregularities produced by internal gravity waves, *J. Atmos. Terr. Phys.,* **30,** 795–823.

Huang, C.S., Sofko, G.J. & Kelley, M.C., 1998. Numerical simulations of midlatitude ionospheric perturbations produced by gravity waves, *J. gephys. Res.,* **103,** 6977–6989.

Huba, J.D., Joyce, G. & Fedder, J.A., 2000. Sami2 is another model of the ionosphere (SAMI2): a new low-latitude ionosphere model, *J. geophys. Res.,* **105,** 23 035–23 053.

Iyemori, T. *et al.*, 2005. Geomagnetic pulsations caused by the Sumatra earthquake on December 26, 2004, *Geophys. Res. Lett.,* **32,** L20807.

Kelley, M.C., 1989. *The Earth's Ionosphere, Plasma Physics and Electrodynamics*, International Geophysics Series, Vol. 43, Academic Press, San Diego.

Kherani, E.A., de Paula, E.R. & Bertoni, F.C.P., 2004. Effects of the fringe field of Rayleigh–Taylor instability in the equatorial E and valley regions, *J. geophys. Res.,* **109,** A12310, doi: 10.1029/2003JA010364.

Kherani, A.E., Mascarenhas, M., De Paula E. R., Sobral, J.H.A. & Bertoni F., 2005. A three-dimensional simulation of collisional-interchange-instability in the equatorial-low-latitude ionosphere, *Space Sci. Rev.,* **121**(1–4), 253–269, doi:10.1007/s11214-006-6158-x.

Kherani, A.E., Lognonné, P., Kamath, N., Crespon, F. & Garcia, R. The ionospheric response during the passage of seismic trigerred acoustic waves: non-local analysis, *J. geophys. Res., submitted*.

Lay, T. *et al.*, 2005. The great Sumatra-Andaman earthquake of 26 December 2004, *Science,* **308,** 1127–1133.

Landau, L.D. & Lifšitc, E.M., 1975. *Mechanika*, Mir, Moscow.

Le Pichon, A., Herry, P., Mialle, P., Vergoz, J., Brachet, N., Garces, M., Drob, D. & Ceranna, L., 2005. Infrasound associated with 2004–2005 large Sumatra earthquakes and tsunami, *Geophys. Res. Lett.,* **32,** L19802, doi: 10.1029/2005GL023893.

Liu, J.Y., Tsai, Y.B., Chen, S.W., Lee, C.P., Chen, Y.C., Yen, H.Y., Chang, W.Y. & Liu, C., 2006a. Giant ionospheric distrubances excited by the M9.3 Sumatra earthquake of 26 December 2004, *Geophys. Res. Lett.,* **33,** L02103, doi: 10.1029/2005GL023963.

Liu, J., Tsai, Y., Ma, K., Chen, Y., Tsai, H., Lin, C., Kamogawa, M. & Lee, C., 2006b. Ionospheric GPS total electron content (TEC) disturbances triggered by the 26 December 2004 Indian Ocean tsunami, *J. geophys. Res.,* **111,** A05303, doi: 10.1029/2005JA011200.

Lognonné, P., Clévédé, E. & Kanamori, H., 1998. Computation of seismograms and atmospheric oscillations by normal-mode summation for a spherical earth model with realistic atmosphere, *Geophys. J. Int.,* **135,** 388–406.

Lognonné, P. *et al.*, 2006. Ground based GPS imaging of ionospheric post-seismic signal, *Planet. Space Sci.,* **54,** 528–540.

Lowes, F.J., 2005. The International Geomagnetic Reference Field: a health warning, http://www.ngdc.noaa.gov/IAGA/vmod/igrfhw.html.

Nappo, C.J., 2002. An introduction to atmospheric gravity waves, in *International Geophysics Series*, Vol. 85, Academic Press, San Diego.

Occhipinti, G., 2006. Observations multi-paramètres et modélisation de la signature ionosphérique du grand séisme de Sumatra, *PhD thesis*, Institut de Physique du Globe de Paris, December 2006, http://www.gps.caltech.edu/∼ninto.

Occhipinti, G., Lognonné, P., Kherani, E.A. & Hebert, H., 2006. Three-dimensional waveform modeling of ionospheric signature induced by the 2004 Sumatra tsunami, *Geophys. Res. Lett.,* **33,** L20104, doi: 10.1029/2006GL026865

Ogawa, T., Balan, N., Otsuka, Y., Shiokawa, K., Ihara, C., Shimomai, T. & Saito, A., 2002. Obsevations and modeling of 630 nm airglow and electron content associated with traveling ionospheric distiurbances aver Shigaraki, Japan, *Earth Planet. Space,* **54,** 45–56.

Okal, E.A., Piatanesi, A. & Heinrich, P., 1999. Tsunami detection by satellite altimetry, *J. geophys. Res.,* **104,** 599–615.

Park, J., Anderson, K., Aster, R., Butler, R., Lay, T. & Simpson, D., 2005. Global Seismographic Network records the Great Sumatra-Andaman earthquake, *EOS, Trans. Am. geophys. Un.,* **86**(6), 57.

Peltier, W.R. & Hines, C.O., 1976. On the possible detection of tsunamis by a monitoring of the ionosphere, *J. geophys. Res.,* **81**(12), 1995–2000.

Picone, J.M., Hedin, A.E., Drob, D.P. & Aikin, A.C., 2002. NRLMSISE-00 empirical model of the atmosphere: Statistical comparisons and scientific issues, *J. geophys. Res.,* **107** (A12), 1468, doi:10.1029/2002JA009430.

Saito, A., Nishimura, M., Yamamoto, M., Fukao, S., Tsugawa, T., Otsuka, Y., Miyazaki, S. & Kelley, M.C., 2002. Observations of traveling ionospheric disturbances and 3-m scale irregularities in the nighttime F-region ionosphere with the MU radar and a GPS network, *Earth Planet. Space,* **54,** 31–44.

Satake, K., 2002. Tsunamis, in *International Handbook of Earthquake and Engineering Seismology*, Part A, Int. Geophys. Ser., Vol. 81A, pp. 437–451, eds Lee, W.H.K., Kanamori, H., Jenning, P.C. & Kisslinger, C., Academic press, San Francisco.

Schunk, R.W. & Nagy, A.F., 2000. *Ionospheres*, Cambridge University Press, Cambridge.

Smith, W., Scharroo, R., Titov, V., Arcas, D. & Arbic, B., 2005. Satellite altimeters measure Tsunami, *Oceanography,* **18**(2), 102, 11–13.

Song, Y., Tony, Chen Ji, L.-L. Fu, Victor Zlotnicki, Shum, C.K., Yuchan Yi and Vala Hjorleifsdottir, 2005. The 26 December 2004 tsunami source estimated from satellite radar altimetry and seismic waves, *Geophys. Res. Lett.,* **32,** L20601, doi: 10.1029/2005GL023683.

Spiegel, E.A. & Veronis, G., 1960. On the Boussinesq approximation for a compressible fluid, *Astrophys. J.,* **131,** 442–447.

Sun, L., Wan, W., Ding, F. & Mao, T., 2007. Gravity wave propagation in the realistic atmosphere based on a three-dimensional transfer function model, *Ann. Geophys.,* **25,** 1979–1986.

Tanaka, T., Ichinose, T., Okuzawa, T., Shibata, T., Sato, Y., Nagasawa, C. & Ogawa, T., 1984. HF-Doppler observation of acoustic waves excited by the Urakawa-Oki earthquake on 21 March 1982, *J. Atmos. Terr. Phys.,* **46**(3), 233–245.

USSA, 1976. U.S. Standard Atmosfere, Committee on the Extantion of the Standard Atmosphere, U.S. Government printing Office, Washington DC.

Vigny, C. *et al.*, 2005. Insight into the 2004 Sumatra-Andaman earthquake from GPS measurement in southeast Asia, *Nature,* **436,** 201–206.

APPENDIX A: ISOTHERMAL CASE

In the case of an isothermal atmosphere, the propagation of internal gravity waves generated at the ground level has an analytical solution (Nappo 2002). In this case, the atmospheric density takes the form

$$\rho(z) = \rho_0 \mathrm{e}^{-z\frac{g}{RT_A}} = \rho_0 \mathrm{e}^{-\frac{z}{H_0}}, \tag{A1}$$

where R is the universal gas constant for dry air, T_A is the average value of the isothermal atmosphere ($\approx$273 K), ρ_0 the initial density at the base of the atmosphere (1.225 kg m^{-3}) and $H_0 = RT_A/g$ the isothermal high scale of the atmosphere. For the standard atmosphere $H_0 = 8$ km (USSA 1976).

In the isothermal approximation the vertical wave vector k_z is determinated by the horizontal wave vector k_x and the angular frequency ω of the tsunami at the sea level,

$$k_z^2 = k_x^2\left(\frac{g}{H_0\omega^2} - \frac{1}{4k_x^2H_0^2} - 1\right).$$

Consequently, the solution of the vertical velocity perturbation produced by the tsunami in the atmosphere take the form

$$u_z(z,t) = u_{z0}e^{\frac{z}{2H_0}}e^{-i(k_z z+\omega t)}.$$

The vertical velocity perturbation produced by the tsunami at the sea surface ($z = 0$) can be used as initial boundary condition of our numerical propagator. In this case, the realistic atmosphere from the empirical model NRLMSISE-00 (Picone *et al.* 2002) can be replaced by the isothermal atmosphere based on eq. (A1) in order to numerically reproduce the isothermal analytical solution. The analytical and numerical solution are compared in Fig. A1, for $t = 0$ and $u_{z0}\sqrt{\rho_0} = 1$, to prove the validity of our propagator.

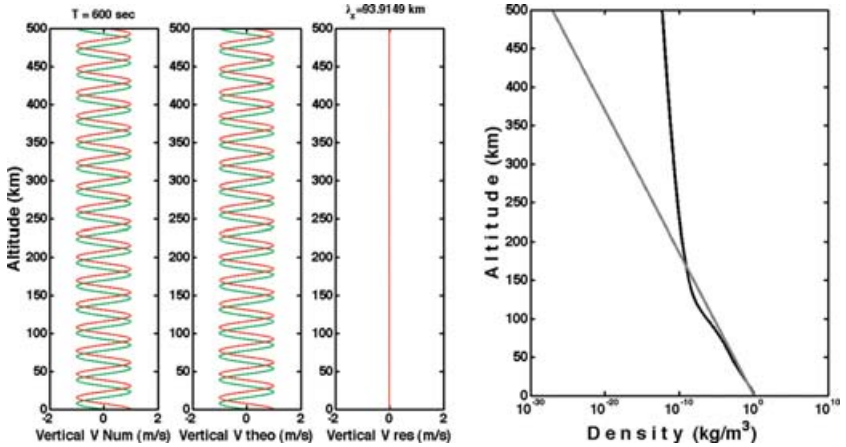

Figure A1. Three left-hand panels: Vertical velocity modes $u_z\sqrt{\rho_0}$ obtained by the numerical propagator and the analytical solution in the left and centre panels, respectively. The difference between the analytical and numerical solution is shown on the right-hand panel. Imaginary (green) and real (red) part of the modes are shown, in the right-hand panel the two lines are superimposed. Right-hand panel: isothermal density of the atmosphere obtained from eq. (A1) (grey) compared with the realistic atmosphere from NRLMSISE-00 empirical model (black).

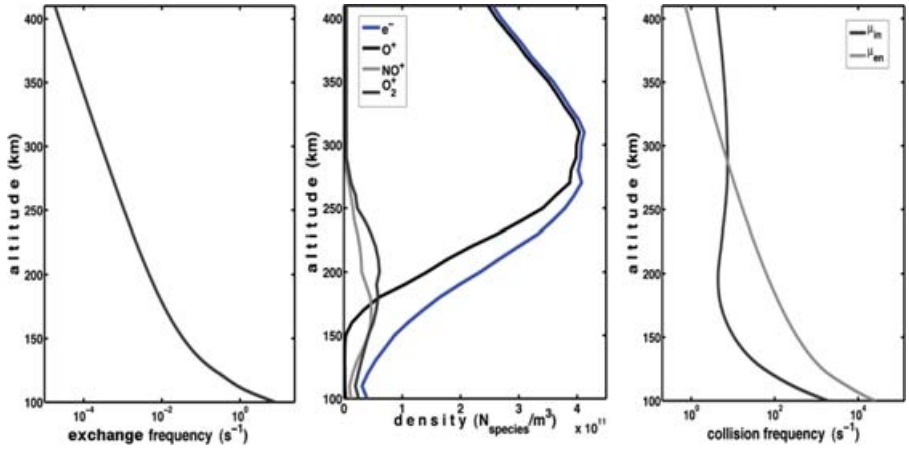

Figure A2. Ionospheric parameter profiles: Ion-molecular exchange frequency β (left-hand panel); the three ion species, O^+, NO^+, O_2^+ and electron e^- densities (central panel); the neutral-ion μ_{in} and neutral-electron μ_{en} collision frequencies (right-hand panel).

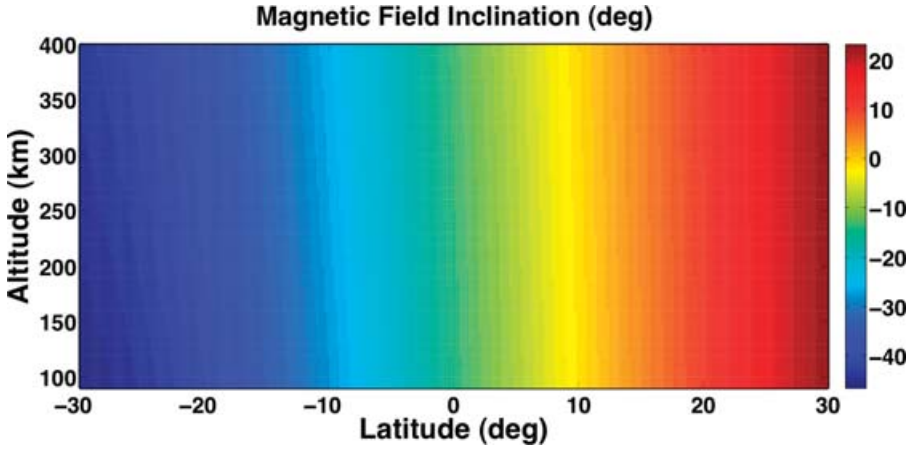

Figure A3. Magnetic field inclination from geomagnetic global model IGRF. The magnetic inclination is shown at 0° longitude. At this longitude the magnetic equator is located near 10° of latitude.

APPENDIX B: GEOMAGNETIC AND IONOSPHERIC PARAMETERS

The 3-D ionospheric and geomagnetic models (parameters and background) used in the plasma eqs (7)–(9) are based on the IRI model (Bilitza 2001) for ions n_i and electron n_e densities; on the SAMI model (Huba *et al.* 2000) for exchange frequency β and α, collision frequencies μ_{in} and μ_{en}; and on the IGRF model for the geomagnetic field (Lowes 2005). These parameters are shown here with respect to the altitude (Fig. A2). The only fixed parameter in the ionospheric modelling is α, its value is 1.67×10^{-13} m^3 s^{-1}.

We note that the electron density n_e and the electron-neutral collision frequency μ_{en} are shown here only for general discussion. The electrons are not explicitly included in our computation but instead their value n_e is obtained from the plasma neutral hypothesis (9).

As described in the main text and in accordance with the literature (e.g. Schunk & Nagy 2000), our ionospheric model is based on the dynamic evolution of the three ions O^+, NO^+, O_2^+ constituting the main ionosphere (Fig. A2). We emphasize that the major perturbation is observed in the O^+ density constituting the F region, where the tsunamigenic ionospheric perturbations were principally observed.

In the Fig. A3, the magnetic inclination from the geomagnetic global model IGRF (Lowes 2005) is shown at the longitude 0° and with respect to the geographical latitude and ionospheric altitude. The magnetic inclination showed here is used in the 2-D modelling presented in the main text. The magnetic inclination plays a a major role in the neutral–plasma coupling, as well as in the background structure of the ionosphere (e.g. the equatorial anomaly Schunk & Nagy 2000).

SUPPLEMENTARY MATERIAL

The following supplementary material is available for this article:

Supplement S1. IGW northward propagation in the neutral atmosphere (S1), northward propagation in the ionosphere (S2) and southward propagation in the ionosphere (S3). The three movies (MPG format) are the extension of Figs 5, 6 and 8 (main body of the text) respectively.

This material is available as part of the online article from: http://www.blackwell-synergy.com/doi/abs/10.1111/j.1365-246X.2008.03760.x
(this link will take you to the article abstract).

Please note: Blackwell Publishing are not responsibe for the content or functionality of any supplementary materials supplied by the authors. Any queries (other than missing material) should be directed to the corresponding author for the article.